nature communications

Article

https://doi.org/10.1038/s41467-024-54834-6

RNA 3′end tailing safeguards cells against products of pervasive transcription termination

Received: 31 March 2024

Accepted: 22 November 2024

Published online: 01 December 2024

Check for updates

Guifen Wu[1], Jérôme O. Rouvière[1], Manfred Schmid[1,2] & Torben Heick Jensen[1]

Premature transcription termination yields a wealth of unadenylated (pA⁻) RNA. Although this can be targeted for degradation by the Nuclear EXosome Targeting (NEXT) complex, possible backup pathways remain poorly understood. Here, we find increased levels of 3′ end uridylated and adenylated RNAs upon NEXT inactivation. U-tailed RNAs are mostly short and modified by the cytoplasmic tailing enzymes, TUT4/7, following their PHAX-dependent nuclear export and prior to their degradation by the cytoplasmic exosome or the exoribonuclease DIS3L2. Longer RNAs are instead adenylated redundantly by enzymes TENT2, PAPOLA and PAPOLG. These transcripts are either degraded via the nuclear Poly(A) tail eXosome Targeting (PAXT) connection or exported and removed by the cytoplasmic exosome in a translation-dependent manner. Failure to do so decreases global translation and induces cell death. We conclude that post-transcriptional 3′ end modification and removal of excess pA⁻ RNA is achieved by tailing enzymes and export factors shared with productive RNA pathways.

Mammalian genomes are pervasively transcribed by RNA polymerase II (RNAPII), yielding functional 5′end capped RNA along with a vast abundance of processing and transcriptional by-products[1,2]. Given this wealth of RNA there is a high demand for efficient turnover of excess transcripts and various decay pathways have evolved to maintain RNA homeostasis by clearing cells of differently sized transcripts[3,4].

In the cytoplasm, the major pathways to control levels of translation-competent RNA involve 5′−3′ exonucleolysis, of prior decapped RNA, by the XRN1 ribonuclease as well as 3′−5′ exonucleolysis by the RNA exosome, via its cytoplasm-specific exonuclease DIS3L[5,6] and its activating Superkiller (SKI) adapter complex[7–9]. RNAs undergoing such decay are most often 3′end processed and polyadenylated in the nucleus and therefore require cytoplasmic deadenylation as a necessary step in their turnover[10,11]. Cytoplasmic RNA control can also occur by its translation-independent 3′end uridylation and subsequent 3′−5′ degradation by DIS3L2, which is independent of the RNA exosome[12–14]. Here, RNA substrates range from certain mRNA to a variety of smaller noncoding RNA (ncRNA), which are uridylated by the uridylyl transferases TUT4 (ZCCHC11) and TUT7 (ZCCHC6)[15–17].

Prior to their cytoplasmic degradation, capped RNAs are exported from the nucleus through different pathways, depending on the RNA species and its features[18,19]. Broadly speaking, the phosphorylated adapter for RNA export (PHAX) is central for the export of short RNA, such as U-rich small nuclear RNA (UsnRNA), perhaps due to the affinity of PHAX for RNAs <300 nt[20–23]. Longer RNAs, including mRNA and long ncRNA, are primarily exported in conjunction by the transcription-export (TREX) complex and the nuclear RNA export factor 1 (NXF1)[24,25].

In the nucleus, decay of capped transcripts is predominantly managed by the 3′−5′ exonucleolytic activity of the RNA exosome, harboring its nuclear-specific subunits DIS3 and RRP6[4,26]. Substrate access is facilitated by the exosome-associated RNA helicase MTR4[27–29], which connects to one of two primary nucleoplasmic adapters: the nuclear exosome targeting (NEXT) complex[30] or the polyA (pA) tail exosome targeting (PAXT) connection[31,32]. NEXT forms a

[1]Department of Molecular Biology and Genetics, Aarhus University, Aarhus, Denmark. [2]Present address: QIAGEN Aarhus A/S, Aarhus, Denmark.
e-mail: thj@mbg.au.dk

dimer of MTR4-ZCCHC8-RBM7 heterotrimers[33,34] and can target the exosome to short, TSS-proximal, pA$^-$ transcripts via its connection to the 5′cap-binding complex (CBC)[35–37]. Conversely, PAXT consists of a core MTR4-ZFC3H1 heterodimer, that associates with the nuclear pA binding protein (PABPN1) to facilitate the exosome-mediated decay of a variety of pA$^+$ RNAs[31,32,38–40]. By their combined targeting of pA$^-$ and pA$^+$ RNAs, NEXT and PAXT are believed to provide for much of the nuclear control of RNAPII-derived transcripts.

The above-mentioned cytoplasmic and nuclear decay pathways have all been characterized in their own rights, but only little is known about the extent to which they functionally crosstalk and/or compensate for one another. This is, however, an important consideration as no pathway will, on its own, be fully sufficient. Moreover, changing gene expression patterns, occurring during cellular transition or upon stress, will unavoidably challenge a specific pathway with the potential hazard of overwhelming it. Finally, certain cellular conditions might affect RNA decay pathway components as exemplified by the NEXT subunit RBM7, which is phosphorylated upon DNA damage, leading to its decreased substrate targeting[41–43]. Here, compensatory pathways are likely required to deal with accumulating NEXT substrates. In one example of NEXT pathway compensation, we previously showed that decreased NEXT activity may allow for the post-transcriptional polyadenylation of formerly pA$^-$ NEXT substrates, leading to their PAXT-dependent nuclear turnover[36]. Hence, this provides one possibility for fail-safe decay in case a first line of substrate recognition is prohibited. However, the cell may contain additional backup mechanisms for NEXT activity. This is because mammalian transcription units (TUs) broadly are prone to premature transcription termination, giving rise to shortened transcripts with either pA$^+$ or pA$^-$ 3′ends[44–46]. Focusing here on pA$^-$ RNAs, which are the targets of NEXT, early RNAPII termination within the first few kilobases (kb) of transcriptional progress is typically directed by the Integrator (INT)- or Restrictor (RES) complexes[47–52]. Since both INT and RES operate genome-wide and in largely sequence-independent manners, extensive amounts of NEXT substrates are constantly being produced.

Here, we explore which decay pathways maintain RNA homeostasis when NEXT-mediated turnover of pA$^-$ RNA is compromised. Focusing on prematurely terminated and promoter upstream transcripts (PROMPTs), we show that a relatively shorter fraction of these are exported, via PHAX, to the cytoplasm, where they are uridylated by TUT4/7 and degraded by the cytoplasmic exosome or the exoribonuclease DIS3L2. The fraction of relatively longer transcripts, escaping NEXT activity, are adenylated redundantly by the TENT2, PAPOLA and PAPOLG enzymes. This yields two possible fates; i) handover in the nucleus for PAXT-mediated decay, or ii) nuclear export by PHAX and the conventional mRNA export machinery and turnover by the cytoplasmic exosome.

Results

Relatively short 3′end uridylated RNAs accumulate upon NEXT- and exosome-depletions

Inspired by our previous discovery that pA$^-$ RNA substrates can undergo post-transcriptional polyadenylation in NEXT and exosome depletion conditions[36], we wondered whether other 3′end modifications might also occur. Hence, we scrutinized previous RNA 3′end sequencing (3′end seq) data[36], taking advantage of their in vitro polyadenylation by *E. coli* poly(A) polymerase (E-PAP), enabling the detection of non-canonical tails (Supplementary Fig. 1a). To obtain a general overview, we first combined data from four different siRNA knockdown conditions (siGFP, siRRP40 (also called siEXOSC3), siZCCHC8 and siZFC3H1) each containing biological triplicate steady-state (“total”) RNA samples, and duplicate RNA samples labeled with 4-thiouridine (“4sU”) for 10 min. From these data, non-aligned terminal sequences were collected and stratified by length, nucleotide content, and the total number of reads computed. Filtering canonical pA tails from the analysis (see “Methods”), the interrogated RNAs contained a variety of non-templated tails, with “mixed A-tails” of occasional non-adenosine residues residing inside pA tails (i.e., A_nG, A_nU, A_nC) and pure U-tails (U_n) being the most abundant (Supplementary Fig. 1b). Although, one should be mindful about possible sequencing artefacts, similar observations were also made using different RNA sequencing techniques, such as TAIL-seq and 3′RACE-seq[53,54], with mixed A-tails and U-tails reported to be synthesized by non-canonical pA polymerases TENT4A/B[53,55,56] and terminal uridylyl transferases TUT4/7[57–59], respectively.

We decided to focus our efforts on U-tailing. To evaluate the extent to which U-tails might constitute sequencing artifacts, we first scored their detection frequencies in cellular RNA compared to that of the spike-in RNA lacking 3′end U-residues (Supplementary Fig. 1a). Cellular RNAs with 1-2 non-templated U’s were significantly, but only marginally better, detected than non-uridylated spike-in RNAs, while the difference became more prominent for RNAs with ≧ 3 non-templated U’s (Supplementary Fig. 1c). The lower detection-specificity for 1-2 U’s might relate to sequencing errors at read ends and/or other unknown technical issues[60,61]. Regardless the cause, we subsequently focused on RNAs with 3-9 residues long U-tails and measured their frequencies in response to depletion of the RNA exosome or its nucleoplasmic NEXT- and PAXT-adapters. Notably, individual depletion of both the RNA exosome subunit RRP40 (siRRP40), and the NEXT component ZCCHC8 (siZCCHC8), led to increased cellular RNA U-tail frequencies of both total- and 4sU-RNA samples in an E-PAP-specific manner (Fig. 1a). Conversely, depletion of the PAXT component ZFC3H1 (siZFC3H1) only affected 4sU RNA U-tail frequencies slightly. To directly visualize RNA U-tail abundance, we constructed aggregate plots, displaying their $\log_2$-transformed sequencing coverage ($\log_2$(cov)) when anchored to all annotated transcription start sites (TSSs). Similar to the frequency measurements, RNA U-tail abundance was increased upon exosome- and NEXT-depletions, but only mildly in 4sU RNA samples upon PAXT-depletion (Fig. 1b). The fact that RNA U-tails were less upregulated in NEXT- *vs.* exosome-depletion conditions, when interrogating total RNAs, but reached similar levels in 4sU RNA samples, was reminiscent of our previous observation for other NEXT-sensitive targets, such as PROMPTs[30,35,36]. This presumably reflects a redundancy between NEXT and PAXT, where NEXT substrates can be polyadenylated and subjected to PAXT-mediated exosome decay[36]. The similar observation for U-tailed RNA indicated multiple layers of RNA quality control.

To analyze for a potential RNA biotype specificity underlying the observed U-tailing, we generated biotype-stratified heatmaps of the 3′ end seq data. Distinctly, increased U-tail levels were observed for all RNA biotypes in exosome- and NEXT-depletion conditions, and in both total- and 4sU-RNA samples (Fig. 1c and Supplementary Fig. 1d). However, compared to the general upregulation of RNA (“all 3′ends”), U-tailing was predominantly present on shorter RNAs. In this relation, we note that transcripts <100nt were excluded from our libraries due to the utilized RNA purification method, which therefore is likely to underestimate RNA U-tail frequencies. Focusing on well-defined NEXT-sensitive PROMPTs[36], a similar pattern of upregulation of relatively short RNAs with U-tails upon exosome- and NEXT-depletion was evident (Fig. 1d). Like the general 3′end heterogeneity of NEXT-sensitive PROMPTs[36], U-tailed transcripts also presented diverse 3′ends (Fig. 1e and Supplementary Fig. 1e).

Taking our analysis together, we conclude that RNA U-tailing is pervasive and generally more abundant upon disruption of the NEXT/exosome pathway. Hence, when NEXT activity is low, RNAs appear, which can both be uridylated and adenylated[36].

Relatively short excess NEXT substrates are uridylated by TUT4/7 and degraded by cytoplasmic exonucleases

In human cells, RNA terminal uridylyl transferase activity is mainly mediated by the TUT4 and TUT7 enzymes, which uridylate RNAs

https://doi.org/10.1038/s41467-024-54834-6

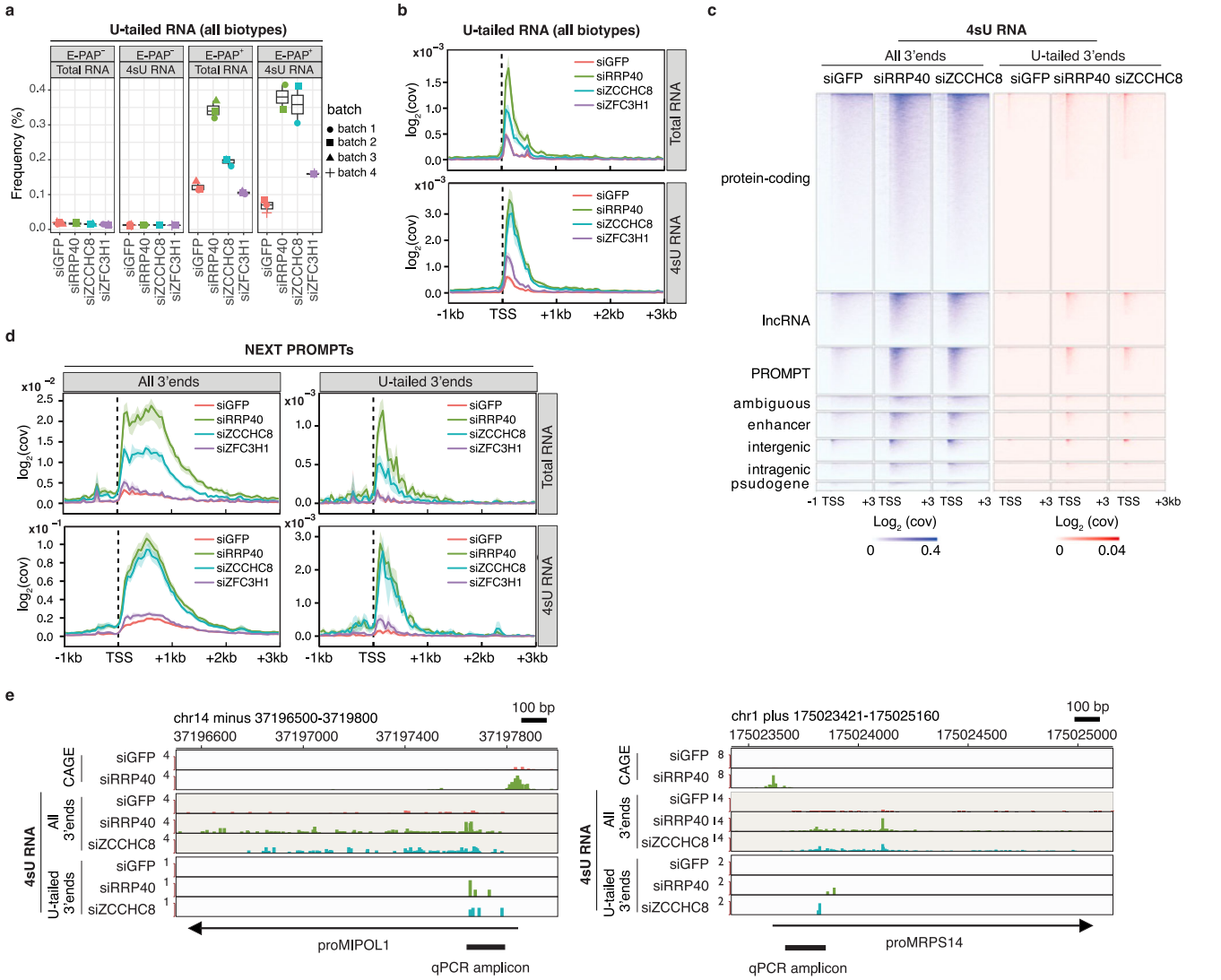

Fig. 1 | The human transcriptome pervasively generates short 3′end uridylated RNAs. a Frequencies of U-tailed RNA as defined by the ratio of reads with non-templated Us ($3 \le U \le 9$) and total RNA reads. Data samples from cells transfected with siRNAs against GFP (siGFP, control), RRP40 (siRRP40), ZCCHC8 (siZCCHC8) or ZFC3H1 (siZFC3H1) are shown (GEO: GSE137612,[36]). Data from samples without (E-PAP$^-$) or with (E-PAP$^+$) in vitro E-PAP treatment are shown separately. Note that all samples were subjected to reverse transcription using a dT primer. The displayed data constitute three biological replicates of total RNA, and two biological replicates of 4sU RNA (10 min labeling) from each of the depletion conditions, except for siGFP/4sU-RNA which was included in triplicate. Sequencing batch numbers are shown on the right. Data are presented as boxplots showing quartiles and with individual batches displayed as separate points. **b** Aggregate plots of reads of cellular U-tailed RNAs from total- and 4sU-RNA samples as indicated. The $\log_2$ data coverage ($\log_2$(cov)) was plotted from regions encompassing −1kb upstream to 3 kb downstream of annotated transcription start sites (TSSs)[50]. Mean values and 90% confidence intervals are shown. The data were normalized to levels of highly expressed mRNAs as previously described[36]. **c** Heatmaps of transcript end sites (TESs) of all RNAs ("All 3′ends") or U-tailed RNAs ("U-tailed 3′ends") from −1kb to 3 kb regions relative to the TSSs of the indicated RNA biotypes as defined in ref. 50. Data from 4sU RNA samples are shown. All heatmaps were sorted in descending order according to the $\log_2$(cov) values in each depletion sample. **d** Metagene profiles as in (b), but showing "All 3′ends" (left) or "U-tailed 3′ends" (right) of NEXT-sensitive PROMPTs split by total (upper) and 4sU (lower) RNA samples. **e** Genome browser views of "All 3′end" and "U-tailed 3′end" data from the indicated 4sU RNA samples. Normalized and averaged signals are shown. PROMPT names (i.e., proMIPOL1 and proMRPS14) are shown at the bottom of each screenshot. RNA 5′end data indicating PROMPT TSSs were derived from cap analysis of gene expression (CAGE) data[119]. qRT-PCR amplicons used for downstream analyses are indicated.

redundantly, but also with substrate preference, to convey RNA processing or degradation[57,58,62,63]. With this in mind, we wondered whether TUT4 and/or TUT7 could uridylate NEXT-sensitive RNAs and control their abundance in the absence of functional nuclear exosome- or NEXT complexes. Hence, siRNAs targeting TUT4 and TUT7 individually, or in combination, were transfected into HeLa cells, expressing RRP40 with a mini-auxin-inducible degron tag (RRP40-mAID), enabling rapid protein depletion upon the addition of indole-3-acetic acid (IAA/auxin)[64] (Supplementary Fig. 2a, b). TSS-proximal PCR amplicons for 8 NEXT-sensitive PROMPTs were designed, based on our RNA 3′end seq data (see examples in Fig. 1e), and used to monitor the relative RNA abundance by qRT-PCR. Given the heterogeneity of the interrogated substrates, a mixture of random hexamer- and anchored dT_{20} (dT_{20}.VN)-primers were utilized for cDNA synthesis to convert all RNA isoforms for subsequent qPCR analysis. Combined depletion of TUT4 and TUT7 (TUT4/7) mildly affected PROMPT levels, which was exacerbated when RRP40 was co-depleted by auxin addition (Supplementary Fig. 2c). A similar trend was observed in a background of ZCCHC8-mAID cells upon their induced ZCCHC8 depletion (Supplementary Fig. 2d–f). We interpret these results to indicate that NEXT and the nuclear exosome normally clear most of the measured substrates, but upon

https://doi.org/10.1038/s41467-024-54834-6

NEXT/exosome inactivation TUT4/7 contributes to suppressing RNA levels.

To more precisely pinpoint how TUT4/7 depletions affected tailing of the interrogated RNAs, we devised a method to semi-selectively measure U-tailed RNA frequencies. Briefly, total cellular RNA was mixed with two in vitro transcribed spike-in RNA species: i) spike-in RNA $1^{\#}$; a mixture of 6 RNA isoforms containing 0 to 5 Us at their 3′ ends, and ii) spike-in RNA $2^{\#}$; a negative control RNA devoid of 3′ terminal Us (Supplementary Fig. 2g). This RNA cocktail was polyadenylated by E-PAP and subjected to reverse transcription using a dT_{20}-A_4 primer for detection of U-tailed RNA (>3U) by subsequent qPCR analysis. The dT_{20}-A_4 primer was tested together with other primers (see details in "Methods") and chosen due to its high specificity for spike-in $1^{\#}$ RNA (observed U-tailed RNA frequency of 22% and close to the theoretical value of 20%) and low detection of the spike-in $2^{\#}$ control (~2%) (Supplementary Fig. 2h). In parallel, levels of all RNA isoforms were measured from cDNA synthesized with the unselective dT_{20}-VN primer, which allowed the calculation of U-tailed RNA frequencies. Gratifyingly, using this E-PAP-based approach to measure levels of all RNA isoforms (Fig. 2a) recapitulated our results using random hexamer- and dT_{20}-VN-primers (Supplementary Fig. 2c). Furthermore, a significant decrease of U-tailed RNA frequencies was

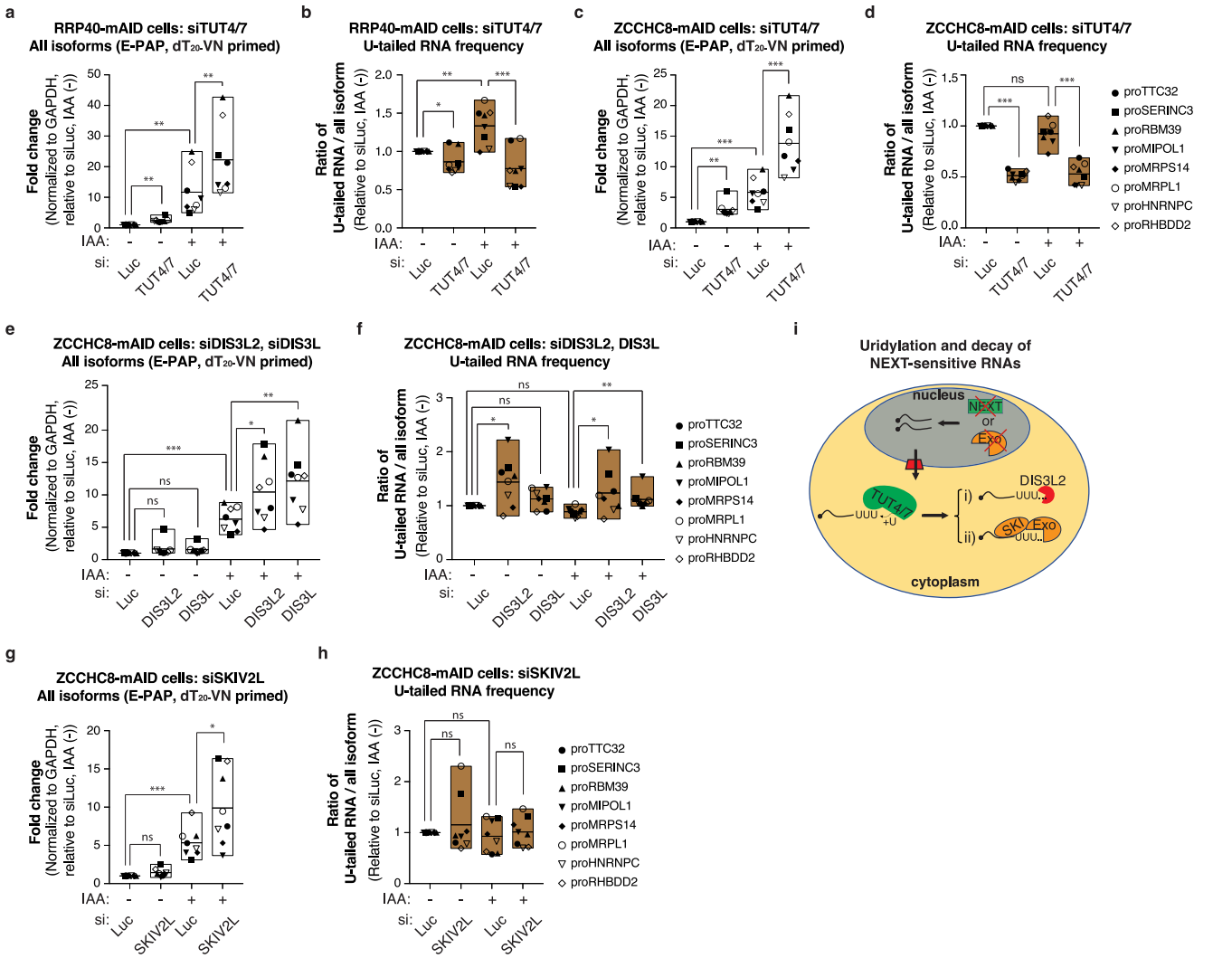

Fig. 2 | Cytoplasmic 3′–5′ exoribonucleases degrade NEXT-sensitive RNAs uridylated by TUT4/7. a Boxplots of qRT-PCR analysis of NEXT-sensitive RNAs from RRP40-mAID cells, transfected with siLuc or siTUT4/7, and treated with auxin (+), or not (−), as indicated. cDNA was synthesized using a dT_{20}-VN primer after E-PAP treatment of total RNA. Individual levels of the 8 RNAs (see right part of Fig. 2d) are represented by separate symbols with the mean value of three biological replicates shown. The line inside each box represents the mean value of the 8 targets. Boxplots display the distribution of the values of 8 targets. All subsequent boxplots are presented similarly. qRT-PCR data were normalized to GAPDH (reference RNA) and plotted relative to the control sample (siLuc, IAA (−)). Statistical analysis was performed using two-sided *t*-tests on the mean values of the 8 targets across samples. * $p < 0.05$; ** $p < 0.01$; *** $p < 0.001$; ns, not significant. Similar statistical tests were conducted for the subsequent qRT-PCR analyses and with *p*-values represented in the same manner. Note that as the siLuc −IAA and siLuc +IAA samples were also produced in Fig. 3a, statistical analysis was performed combining data from all experiments (see "Methods"). All subsequent qRT-PCR experiments were conducted employing three biological replicates unless stated otherwise. Note that boxplots, which display measurements of all RNA isoform levels ("All isoforms") after E-PAP treatment and dT_{20}-NV priming condition, are consistently represented in white color. **b** Boxplots of qRT-PCR analysis of U-tailed RNA frequencies as described in Supplementary Fig. 2g. Note that boxplots, which display measurements of U-tailed RNA frequencies, are consistently represented in brown color. **c** Boxplots of qRT-PCR analysis as in (**a**), but employing ZCCHC8-mAID cells. **d** Boxplots of qRT-PCR analysis of U-tailed RNA frequencies as in (**b**), but employing ZCCHC8-mAID cells. **e** Boxplots of qRT-PCR analysis as in (**c**), but employing siDIS3L2 or siDIS3L siRNAs as indicated. **f** Boxplots of U-tailed RNA frequencies analysis as in (**d**), but employing siDIS3L2 or siDIS3L siRNAs as indicated. **g** Boxplots of qRT-PCR analysis as in (**c**), but employing siSKIV2L siRNA as indicated. **h** Boxplots of U-tailed RNA frequencies analysis as in (**d**), but employing siSKIV2L siRNA as indicated. **i** Diagram summarizing the proposed uridylation and decay pathway.

detected upon TUT4/7 depletion, consistent with the uridylyltransferase activities of these enzymes (Fig. 2b). As expected, similar phenotypes were observed in ZCCHC8-mAID cells upon depleting TUT4/7 (Fig. 2c-d).

How do these U-tailed RNAs get degraded? As TUT4/7 localize to the cytoplasm of human cells[54,65], we focused on three possible cytoplasmic decay pathways; i) 3′−5′ RNA decay by DIS3L2, ii) 3′−5′ decay by the cytoplasmic exosome, represented by DIS3L, and iii) 5′-3′ RNA decay by XRN1. Individual siRNA-mediated depletion of these RNA exonucleases was carried out in ZCCHC8-mAID cells (Supplementary Fig. 2i, j). Scrutinizing levels of all RNA isoforms established that depletion of either DIS3L2 or DIS3L, but not XRN1, increased transcript levels in ZCCHC8 depletion conditions (Fig. 2e and Supplementary Fig. 2k). To further evaluate possible roles of DIS3L2 and DIS3L in U-tailed RNA decay, U-tailed RNA frequencies were also measured. In contrast to TUT4/7 depletion conditions, the frequencies of U-tailed RNAs were slightly increased as a result of elevated U-tailed RNA levels (Fig. 2f). To substantiate a role of the cytoplasmic exosome, we also depleted SKIV2L (Supplementary Fig. 2l), a component of its accessory SKI complex[9,66]. Consistent with the effect of DIS3L depletion, SKIV2L depletion also increased transcript levels (Fig. 2g). Due to a proportional increase of U-tailed RNAs, their frequencies remained unchanged (Fig. 2h).

Taking our results together, we conclude that NEXT-sensitive PROMPTs, upon escaping NEXT-mediated nuclear exosome decay, can be exported to the cytoplasm, where at least a fraction of these, can be uridylated by TUT4/7 (Fig. 2i). Uridylated RNAs are then degraded by DIS3L2 or by the cytoplasmic exosome. While an involvement of DIS3L2 in degrading U-tailed RNA is unsurprising[15,63,67,68], the cytoplasmic exosome has not previously been implicated in U-tailed RNA degradation. However, it has been reported to degrade U-tailed nonsense-mediated mRNA decay (NMD) intermediates[69] and SKIV2L can bind U-tailed RNA[66]. Thus, decay of U-tailed RNA by the cytoplasmic exosome could be a more general mechanism.

PHAX exports shorter excess NEXT substrates for cytoplasmic uridylation

We next addressed how the mostly short and excess NEXT substrates end up in the cytoplasm after escaping nuclear decay. Since the PHAX protein is involved in the export of short capped RNA, such as UsnRNA, short ncRNA and the H2AX RNA, due to its affinity for RNA < 300 nt[20–23], we interrogated this possibility by depleting cellular PHAX and subsequently measured all isoform RNA levels and U-tailed RNA frequencies. As observed for siTUT4/7, co-depletion of PHAX with RRP40 significantly increased NEXT-sensitive PROMPT levels (Fig. 3a and Supplementary Fig. 3a), while markedly decreasing U-tailed RNA frequencies (Fig. 3b). Similar tendencies were observed upon co-depletion of PHAX with ZCCHC8 (Fig. 3c, d and Supplementary Fig. 2i). This suggested that PHAX depletion may stabilize these RNAs indirectly by retaining them in the nucleus, avoiding uridylation and decay in the cytoplasm. We note that PHAX depletion on its own impacted RNA levels, which likely attributed to lowered ZCCHC8 levels upon mAID-tagging[64]. Regardless, these data support the idea that PHAX is involved in the nuclear export of relatively short and excess NEXT substrates, which makes them accessible for uridylation in the cytoplasm.

To evaluate PHAX binding to the investigated transcripts, we conducted RNA immunoprecipitation (RIP) using a GFP antibody to precipitate PHAX from HeLa cells, stably expressing a 'localization and affinity purification' (LAP)-tagged PHAX (PHAX-LAP) construct, containing a C-terminal GFP moiety[70,71]. As expected, given the recruitment of PHAX to RNA via the CBC[21], a specific interaction between PHAX-LAP and the CBP20 and CBP80 proteins could be confirmed, which was not affected by ZCCHC8-depletion (Supplementary Fig. 3b). More importantly, the PHAX-LAP IP enriched for NEXT substrates in the control (siLuc) condition, which was further increased upon ZCCHC8 depletion (Fig. 3e), presumably due to increased substrate availability (Supplementary Fig. 3c). We suggest that in the absence of NEXT, more of its RNA substrates bind to PHAX, which mediates their nuclear export, providing for cytoplasmic uridylation-coupled degradation (Fig. 3f).

A fraction of longer excess NEXT substrates is polyadenylated and exported to the cytoplasm

Inspired by shorter excess NEXT substrates, utilizing nuclear export and cytoplasmic U-tailing for their decay, we wondered whether A-tailed excess NEXT substrates would employ a similar backup mechanism, in addition to their demonstrated handover for PAXT-mediated decay in the nucleus[36]. Our RNA 3′end seq data revealed that A-tailed substrates, accumulating upon ZCCHC8 depletion, were generally longer than their U-tailed counterparts (Fig. 4a, compared to Fig. 1d, right panel). Moreover, and as previously shown[36], levels of A-tailed substrates were increased upon co-depletion of ZCCHC8 with the PAXT component ZFC3H1 (Fig. 4a).

Despite the fact that pA$^-$ NEXT-substrates can be polyadenylated, the responsible poly(A) polymerase(s) (PAPs) remained unclear as did the probability of whether a fraction of these A-tailed RNAs could be subjected to nuclear export (Fig. 4b). To address the first question, we depleted canonical PAPs, PAPOLA and PAPOLG, as well as their non-canonical, but nuclear, counterparts TENT1, TENT4A/TENT4B (TENT4A/B) and TENT2 (Supplementary Fig. 4a–c). Individual depletion of TENT2, PAPOLA and PAPOLG mildly increased NEXT substrate levels in the ZCCHC8 depletion condition, but no effect was observed upon TENT1 or TENT4A/B depletion (Supplementary Fig. 4d). To address any possible redundancy, TENT2, PAPOLA and PAPOLG were co-depleted (Supplementary Fig. 4c and Supplementary Fig. 4e), which led to more robust RNA accumulation (Fig. 4c). This was mirrored by a decreased RNA A-tailing frequency (Fig. 4d and Supplementary Fig. 4f). We, therefore, conclude that A-tailing of excess NEXT substrates can be conducted redundantly by TENT2, PAPOLA and PAPOLG.

To next explore the possibility of nuclear export of A-tailed RNAs, their levels were examined by co-depleting candidate export factors with ZCCHC8. PHAX co-depletion increased A-tailed RNA levels (Fig. 4e), which was consistent with its binding to these substrates as demonstrated by RIP experiments (Supplementary Fig. 4g, h). We noted, however, that PHAX binding here was less prominent when compared to its interaction with all RNA isoforms (compare Supplementary Figs. 4h and 3e, note Y-axis scales). Given that most A-tailed RNAs are believed to be exported by NXF1 with the assistance of the TREX complex[18,19,72], we co-depleted NXF1 or the TREX component DDX39A/B (DDX39A/DDX39B) along with ZCCHC8 (Supplementary Fig. 4i, j). Both depletions yielded increased levels of A-tailed RNA (Fig. 4f, g), suggesting that these excess NEXT substrates can also be exported by the TREX-NXF1 pathway, possibly because the nuclear PAXT/exosome decay pathway becomes saturated.

Taking the data together, we suggest that excess NEXT substrates can be redundantly polyadenylated by TENT2, PAPOLA and PAPOLG, leading to PAXT-mediated nuclear decay or PHAX- or TREX-NXF1 mediated export (Fig. 4h). Given that PHAX can also export pA$^-$ RNA, its depletion could potentially make retained pA$^-$ RNAs available for polyadenylation by TENT2/PAPOLA/PAPOLG, which might contribute to the observed phenotype.

Exported A-tailed excess NEXT substrates are degraded in a translation-dependent manner

The observed increase in A-tailed excess NEXT substrates, upon export factor depletion, suggested their removal in the cytoplasm. To interrogate by which mechanism(s) such decay might be carried out, we examined A-tailed substrate levels from ZCCHC8-mAID samples co-depleted for the exosome exoribonuclease DIS3L, or

https://doi.org/10.1038/s41467-024-54834-6

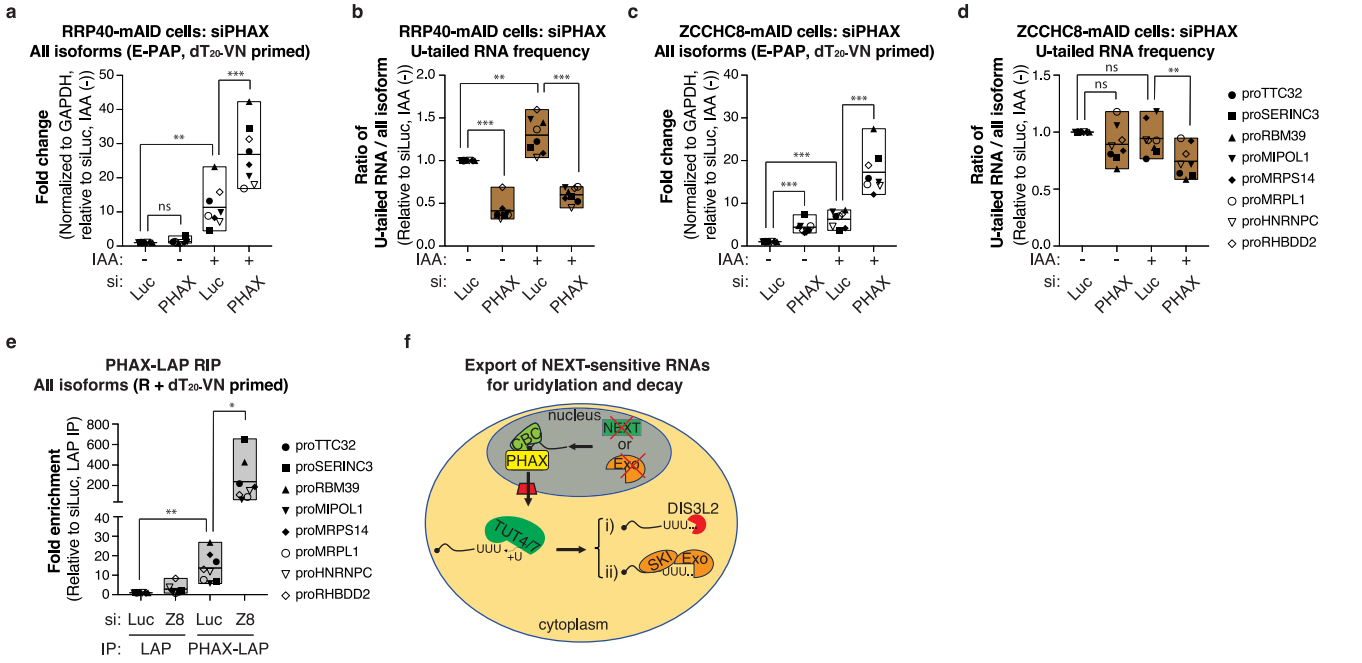

Fig. 3 | PHAX exports NEXT-sensitive RNAs for cytoplasmic uridylation. **a** Boxplots of qRT-PCR analysis as in Fig. 2a, but depleting PHAX. **b** Boxplots of U-tailed RNA frequencies as in Fig. 2b, but depleting PHAX. **c** Boxplots of qRT-PCR analysis as in (**a**), but employing ZCCHC8-mAID cells. **d** Boxplots of U-tailed RNA frequencies as in (**b**), but employing ZCCHC8-mAID cells. **e** Boxplots of qRT-PCR analysis of the indicated RNA levels from IP samples from Supplementary Fig. 3b. The values of the control sample (siLuc, LAP IP) were set to 1. cDNA for qPCR analysis was synthesized by a mix of random hexamer- and dT_{20}-VN-primers (R + dT_{20}-VN). Given the high reproducibility and limited experimental material, this experiment was conducted with two biological replicates. Note "Z8" is short for ZCCHC8. **f** Diagram summarizing the proposed RNA export, uridylation and decay pathways.

DIS3L2 (Supplementary Fig. 2i). While DIS3L2 depletion, in line with its uracil-specificity[15,67], did not affect A-tailed RNA levels (Supplementary Fig. 5a), these increased upon DIS3L depletion (Fig. 5a). Consistent with an involvement of the cytoplasmic exosome, depleting SKIV2L (Supplementary Fig. 2l) also increased levels of excess A-tailed NEXT substrates (Fig. 5b). Moreover, disrupting both nuclear and cytoplasmic decay by co-depleting ZFC3H1 and SKIV2L (Supplementary Fig. 2l) further increased A-tailed RNA levels (Fig. 5b), suggesting that the two decay pathways cooperate to clear these substrates.

To investigate whether cytoplasmic SKI/exosome degrades excess A-tailed NEXT substrates in a translation-dependent manner, we treated ZCCHC8-mAID cells with the translation elongation inhibitor cycloheximide (CHX). This led to increased levels of A-tailed RNA (Fig. 5c), suggesting translation-dependent turnover, as also observed for other cytoplasmic exosome substrates[9,66,73]. Interestingly, however, although DIS3L dually participates in A-tailed and U-tailed RNA decay (Figs. 2f and 5a), turnover of the latter was not CHX-sensitive (Supplementary Fig. 5b).

The engagement of translation in the turnover of cytoplasmic A-tailed excess NEXT substrates might occupy available ribosomes and, in turn, affect normal translational output. To address this possibility, we estimated protein synthesis by labeling nascent peptides with puromycin, which causes premature chain termination by its covalent incorporation into the growing peptide chain measurable by anti-puromycin western blotting analysis[74–76]. As our ZCCHC8-mAID cells harbor the puromycin resistance gene, we employed regular HeLa cells and instead depleted ZCCHC8 and/or ZFC3H1 by siRNA transfection (Fig. 5d, bottom panels). Individual depletion of these factors led to decreased puromycin levels, which was further lowered by ZCCHC8/ZFC3H1 co-depletion (Fig. 5d, top panel and Fig. 5e). Similar effects were previously observed for ZFC3H1 depletion, but not for ZCCHC8 depletion, which we suspect was due to a lower depletion efficiency than obtained here[38]. In conclusion, excess RNA released from the nucleus negatively impacts global protein synthesis, possibly by occupying the translation machinery. In line with this, overall increases in total pA^+ RNA levels (Supplementary Fig. 5c) inversely correlated with puromycin incorporation (compare Supplementary Fig. 5c and Fig. 5e). Such importance of ZCCHC8 and ZFC3H1 in maintaining normal protein synthesis implied increased cell death upon their depletion, which was validated by flow cytometry analysis, revealing an increased sub-G1 population accompanied by a decreased G0/G1 population (Fig. 5f, g, Supplementary Fig. 5d, e).

Taking these results together, we suggest that A-tailed excess NEXT substrates can either be degraded in the nucleus by the PAXT/exosome pathway or in the cytoplasm by the SKI/cytoplasmic exosome complex in a translation-dependent manner (Fig. 5h). We suggest that this protects against an overpowering of physiological translation and promotes cell survival, although a strict cause and effect relationship still remains to be established.

Fail-safe decay pathways target NEXT substrates upon DNA damage

Our results so far revealed fail-safe removal of NEXT substrates under conditions where this nuclear exosome adapter was artificially depleted. To address whether the identified NEXT backup systems would also respond to other conditions affecting NEXT activity, like DNA damage where RBM7 is phosphorylated and in turn lowers its affinity towards decay substrates[41–43], we challenged cells with 4-nitroquinoline 1-oxide (4-NQO). This chemical triggers DNA damage through its metabolite 4-hydroxyaminoquinoline 1-oxide by forming DNA adducts on purines[77]. As expected, 4-NQO administration increased levels of the previously interrogated "All isoforms" (Fig. 6a, compare siLuc 4-NQO (−) and (+)), consistent with NEXT inactivation[41,43]. Moreover, depleting SKIV2L or DIS3L2 in 4-NQO treated cells (Supplementary Fig. 6) further increased RNA levels (Fig. 6a). We note that U-tailed RNA frequencies decreased following 4-NQO treatment (Fig. 6b). Since 4-NQO triggers RNAPII release from

https://doi.org/10.1038/s41467-024-54834-6

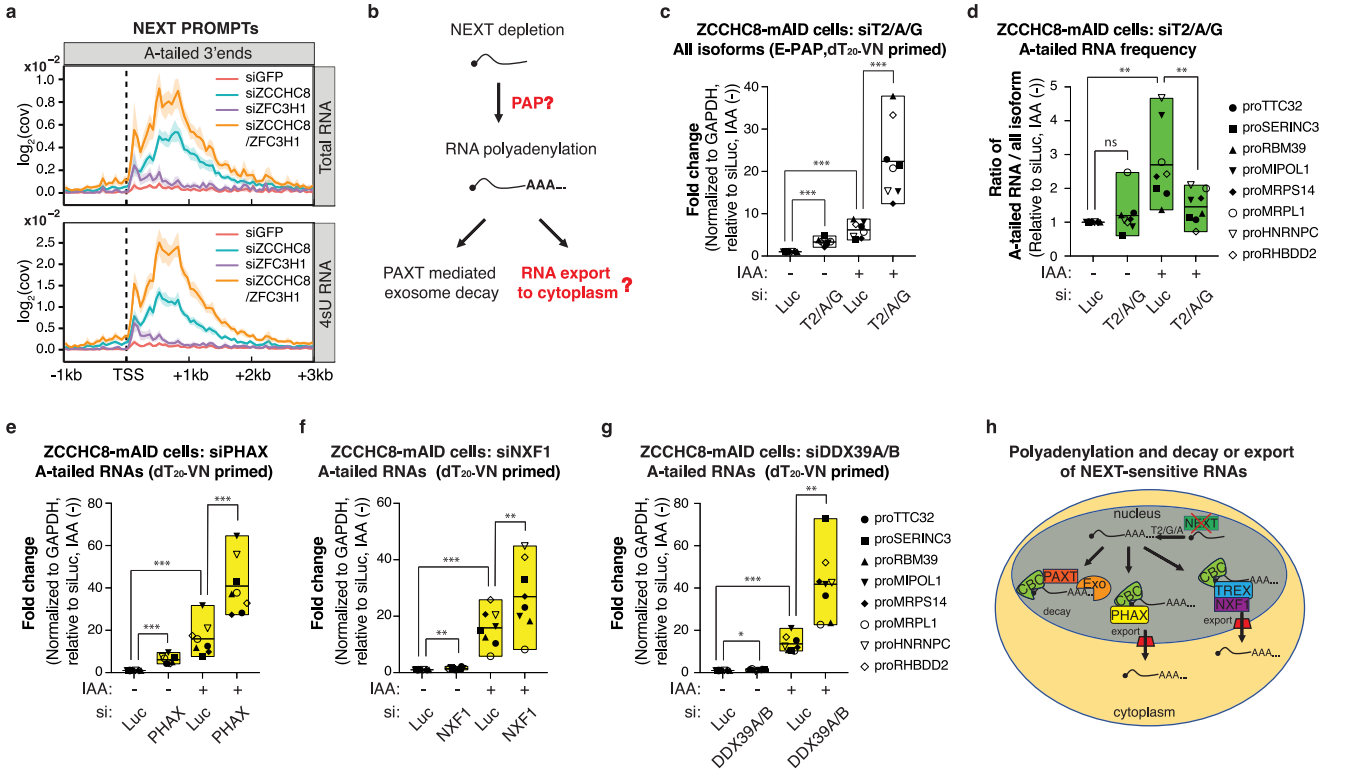

Fig. 4 | NEXT-sensitive RNAs can be polyadenylated and exported to the cytoplasm. a Metagene profiles as in Fig. 1d, but showing 'A-tailed 3'ends' of NEXT-sensitive PROMPTs from the indicated depletion samples, displaying total- (upper) or 4sU- (lower) RNA. Data from no E-PAP treatment samples were used (data in GEO: GSE137612,[36]). **b** Schematic diagram showing the proposed nuclear polyadenylation of excess NEXT substrates followed by their nuclear decay or export. Red text and question marks indicate unresolved processes. **c** Boxplots of qRT-PCR analysis as in Fig. 3c, but depleting TENT2/PAPOLA/PAPOLG (T2/A/G). **d** Boxplots of qRT-PCR analysis of samples from (**c**) but measuring A-tailed RNA frequencies as depicted in Supplementary Fig. 4f. Note that this boxplot, which displays measurements of A-tailed RNA frequencies, is represented in green color. **e** Boxplots of qRT-PCR analysis of A-tailing levels of RNAs from Fig. 3c. To obtain A-tailed RNA, total RNA samples were reverse transcribed with a dT_{20}.VN primer before qPCR analysis. Note that boxplots, which display measurement of A-tailed RNA levels ("A-tailed RNAs":), are consistently represented in yellow color. **f** Boxplots of qRT-PCR analysis as in (**e**), but depleting NXF1. **g** Boxplots of qRT-PCR analysis as in (**e**), but depleting DDX39A/B. **h** Diagram summarizing the proposed PAXT-mediated exosome decay or nuclear export of A-tailed excess NEXT substrates.

promoter-proximal pausing[41], we speculate that fewer short RNAs, which are substrates for uridylation, are produced. Finally, depleting ZFC3H1 or SKIV2L, or both, increased A-tailed RNA levels in 4-NQO treated cells (Fig. 6c), and combining siZFC3H1 with 4-NQO treatment induced a significant increase of sub-G1 populations (Fig. 6d, e). We therefore conclude that fail-safe decay is also operational upon DNA damage.

Discussion

Decay systems rid cells of aberrant and excess transcripts to maintain RNA homeostasis. This encompasses major RNA decay pathways, across the nucleus and the cytoplasm[3,4], but how these interrelate to compensate for one another has not been thoroughly explored. In one example from higher eukaryotes, we have previously described that the inefficient removal of pA$^-$ RNA substrates by the nuclear exosome, due to depletion of its NEXT adapter complex, may trigger their post-transcriptional 3'end adenylation and subsequent handover to PAXT-mediated nuclear decay by the exosome[36]. Earlier data from budding yeast have demonstrated that handover of excess RNA can also occur across cellular compartments as transcripts escaping nuclear quality control are exported and abundantly targeted by the cytoplasmic nonsense-mediated decay (NMD) pathway[78]. In the present study, we expand this principle by describing NEXT pathway backup mechanisms that rely on RNA 3'end tailing and nuclear export mechanisms to achieve cytoplasmic decay (Fig. 3f and Fig. 5h). The need for cells to be able to efficiently handle excess NEXT substrates is apparent given the wide variety of such substrates, including PROMPTs[30], eRNAs[79], 3' extended snRNAs, snoRNAs, histone RNAs and telomerase RNAs[64,79–81] as well as prematurely terminated RNAPII products from within protein-coding genes[47,50–52] and from within transposable elements[82,83]. We, therefore, suggest that primary decay by NEXT/exosome and compensation by backup systems cooperate to restrict these non-productive RNAs, enabling cells to handle extrinsic challenges, such as the DNA damage condition imposed in this study, ultimately promoting cell survival.

Our discovered backup mechanisms involve RNA 3'end tailing, which implies that at least some RNAs with naked 3'ends are not optimal decay substrates after their escape from initial NEXT targeting. In previously reported cases, NEXT complex activity occurs in tight conjunction to the prior processes of transcription termination[50,52,83], pre-mRNA splicing[64,84] or microprocessor cleavage[85] and in select examples, a direct physical interaction between RNA substrate production- and decay systems have been demonstrated[51,52,85]. Thus, while conventional turnover of NEXT substrates is typically a coupled process that accepts an unmodified RNA 3'end, their efficient "pick up" by alternative decay pathways might rely on prior 3'end tailing. For example, RNA uridylation appears to be a prerequisite for decay, as TUT4/7 depletion leads to RNA stabilization (Fig. 3a and c). Similarly, nuclear RNA adenylation is presumably central for translation-coupled decay as poly(A) tails stimulate translation[86]. That said, we cannot exclude that some 3'end tailing may result from the increased availability of non-tailed RNA in conditions where the relevant decay machinery has been compromised. However, we consider this a minor fraction, given the coupling between 3'end tailing and decay.

https://doi.org/10.1038/s41467-024-54834-6

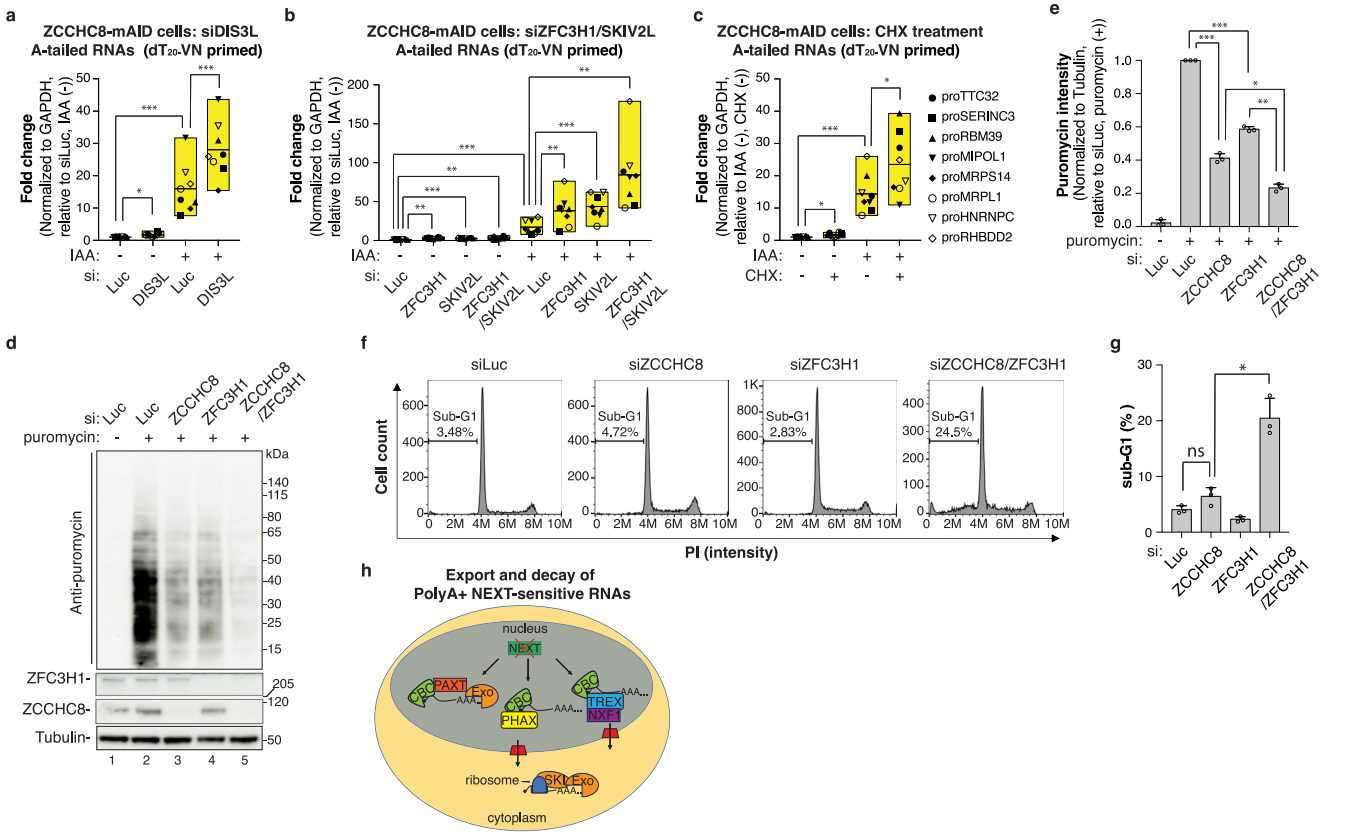

Fig. 5 | SKI/exosome degrades A-tailed NEXT-sensitive RNAs in cytoplasm. **a** Boxplots of qRT-PCR analysis as in Fig. 4e, but employing the indicated samples from Supplementary Fig. 2i. **b** Boxplots of qRT-PCR analysis as in (**a**), but employing the indicated samples from Supplementary Fig. 2l. **c** Boxplots of qRT-PCR analysis as in (**a**), but treating cells without (−) or with (+) 10 ug/ml cycloheximide (CHX) for 3 h. **d** Western blotting analysis assessing puromycin incorporation in cells upon the indicated siRNA-mediated protein depletions. HeLa cells were siRNA transfected for 72 h and treated with 5 ug/ml puromycin for 30 min before harvesting for western blotting analysis. Western membranes were probed with antibodies towards puromycin, ZCCHC8, ZFC3H1, and Tubulin as a loading control. A representative experiment from biological triplicate data is shown. **e** Quantification of triplicate experiments from (**d**). Puromycin signal intensities were normalized to those of Tubulin and with the control sample (siLuc, puromycin (+)) set to 1. Biological triplicate data are shown with each circle representing single replicate values. Error bars represent standard deviations (SDs) and bar graph is presented as mean ± SD. All subsequent bar graphs are presented similarly. **f** Flow cytometry analysis of the cell cycle distribution of cells subjected to the indicated siRNA-mediated protein depletion. The percentages of sub-G1 cells are indicated. A representative experiment from biological triplicate data is shown. **g** Quantification of sub-G1 population data from (**f**). Biological triplicate data are shown with each circle representing single replicate values. **h** Diagram summarizing the proposed nuclear PAXT/exosome decay, export and cytoplasmic SKI/exosome decay of A-tailed excess NEXT substrates.

In the instance of the shorter fraction of our interrogated excess NEXT substrates, cytoplasmic 3′end uridylation proceeds decay by DIS3L2 or the SKI-associated exosome. RNA U-tailing is generally considered a mark for complete RNA decay, although transcript processing might also ensue, e.g., uridylation of U6 snRNA[87–89] and mono-uridylation of *Let-7* miRNA[90–92]. Despite the fact that non-templated U-tails are found on a range of RNA substrates and that the operational uridylation enzymes TUT4 and TUT7 have been identified, the mechanisms underlying TUT4/7 recruitment to RNA 3′ends have only been delineated in a few individual cases. In one example, the *Let-7* miRNA binding protein Lin28 directly interacts with TUT4/7 in embryonic stem cells[93,94], and in another, TUT4/7 targeting to transcripts, deriving from LINE-1 retrotransposable elements, is reported to occur via the MOV10 protein[54]. Since DIS3L2 was found to bind structured RNAs, secondary structure has been suggested to directly, or indirectly through RNA binding proteins, recruit TUT4/7[17]. However, the diverse set of DIS3L2 and SKI-exosome substrates reported in the present study suggests that a more general feature of these transcripts might be recognized. Given the shortness of the identified U-tailed excess NEXT substrates, RNA size might be relevant for TUT4/7 recruitment. Perhaps the difficulty of these RNAs to associate with ribosomes enhances the likelihood of TUT4/7 targeting. This could direct SKIV2L to the U-tailed RNA, either directly[66] or via an intermediary protein, as seen for fungus-specific SKA1 protein[95]. In an alternative, but not mutually exclusive, scenario the nuclear history of these transcripts might impact the involved cytoplasmic processes. In the absence of active NEXT-targeting, the competing process of PHAX-mediated nuclear export prevails[37,70], possibly enabling the resident RNA to be subjected to cytoplasmic 3′end modification as is the case for conventional UsnRNA PHAX-export substrates[96,97]. However, different from the productive 3′end processing and RNP assembly of snRNA prior to their nuclear re-import, excess NEXT substrates are subjected to removal. Which mechanism(s) might discriminate these productive and destructive pathways remains an interesting matter for further investigation.

While RNA U-tailing is primarily involved in destructive pathways, A-tailing is widely employed for both productive and destructive purposes. Conventional 3′end polyadenylation by the cleavage and polyadenylation (CPA) complex largely occurs co-transcriptionally and is critical for further RNA processing, stability, nuclear export, and translation[98–101]. In a countering destructive pathway, the RNA polyA tail and its nuclear pA-binding protein (PABPN1) can direct transcripts for decay by the PAXT/exosome pathway[30–32,36,39,40,102–105]. Additionally, short polyA tails, added by the mammalian Trf4/Air2/Mtr4

https://doi.org/10.1038/s41467-024-54834-6

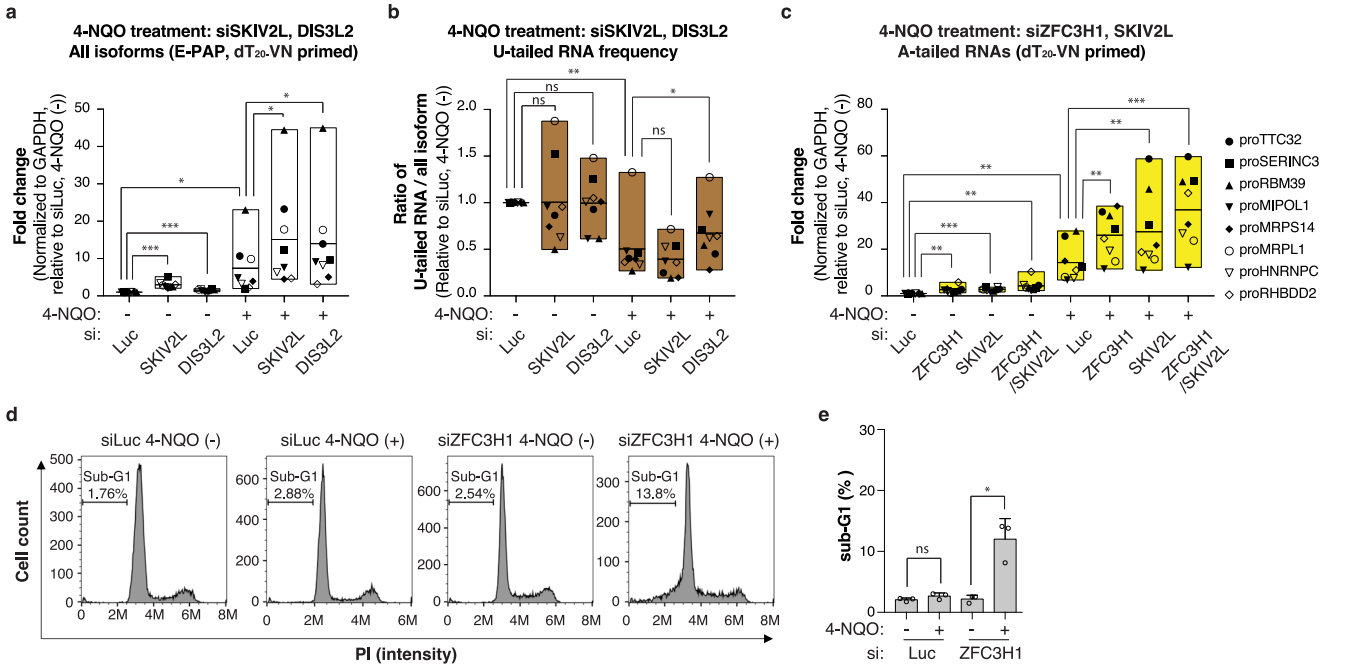

Fig. 6 | Fail-safe pathways degrade NEXT substrates upon DNA damage. **a** Boxplots of qRT-PCR analysis as in Fig. 2a but employing the indicated depletion samples treated with 5 μM 4-NQO (+), or not (−) for 4 h. **b** Boxplots of qRT-PCR analysis as in (**a**), but measuring U-tailed RNA frequencies. **c** Boxplots of qRT-PCR analysis as in Fig. 4e but employing the indicated depletion samples with or without 4-NQO treatment. **d** Flow cytometry analysis as in Fig. 5f, but employing the indicated samples with or without 4-NQO treatment. **e** Quantification of sub-G1 cell populations from (**d**). Biological triplicate data are shown with each circle representing single replicate values.

polyadenylation (TRAMP) complex promote the turnover of rRNA processing byproducts through the nuclear exosome[30,106]. We suggest that in an apparent blend of these pathways, excess NEXT substrates may be A-tailed in the nucleus in preparation for their PAXT-mediated destruction or their PHAX/TREX-NXF1 mediated export ([36] and the present study). Which factors might tilt an RNA towards nuclear decay or export remains unknown. For example, it has been established that PABPN1 functions in the handover of NEXT substrates to PAXT-mediated exosome decay[31,36], but PABPN1 has also been reported to mediate RNA export[107]. Regardless this mechanism, we show that such A-tailing is redundantly conducted by the TENT2, PAPOLA, and PAPOLG enzymes. Again, it is unclear how this might occur. TENT2 is localized in both the nucleus and the cytoplasm[108,109], and was reported to adenylate cytoplasmic mRNA through recruitment by the cytoplasmic polyadenylation element-binding protein 1 (CEBP1) or the QKI7 KH domain-containing RNA binding (QKI-7) protein[110–112]. PAPOLG is strictly nuclear, while PAPOLA is both nuclear and cytoplasmic, and both enzymes are reported to adenylate RNA in a CPA-dependent process coupled to pA site cleavage[113,114]. Since NEXT substrates are originally produced as pA$^-$ RNAs in a CPA-independent manner[36], their adenylation by TENT2, PAPOLA, and PAPOLG in the nucleus is most likely posttranscriptional. Given the localization of TENT2 and PAPOLA, some adenylation could also occur in the cytoplasm. As for 3′end uridylation, additional factors involved in attracting these pA polymerases to their pA$^-$ RNA 3′ends remain to be defined.

We show that export of adenylated excess NEXT substrates is mediated by conventional RNA export factors/complexes PHAX, TREX, and NXF1. This occurs in apparent competition with PAXT-mediated decay, shown here indirectly by the increased overwhelming of general translation upon co-depletion of the PAXT component ZFC3H1 (Fig. 5d), and previously demonstrated directly by nuclear-cytoplasmic fractionation experiments[38,105,115]. The major effects of ZCCHC8 and ZFC3H1 depletions on translation (Fig. 5d) may well underscore the scale of cryptic RNAs normally removed in the nucleus to maintain RNA homeostasis. It also suggests that most of these transcripts, upon entering the cytoplasm, do not produce appreciable amounts of protein but rather block ribosomes, preventing translation of proper mRNA. Cytoplasmic removal of the latter is mainly controlled by the translation-dependent and XRN1 mediated 5′–3′ RNA decay pathway[66,116]. In contrast, the A-tailed excess NEXT substrates reported in this study are predominantly degraded in a translation-mediated process, depending on the SKI/exosome (Fig. 5a, b), but not by XRN1 (Supplementary Fig. 2k). Since the SKI/exosome pathway has been reported to degrade specific transcripts triggering ribosome stalling, such as RNAs with small open reading frames (sORFs)[9,66], particular features of adenylated excess NEXT substrates are likely to elicit their turnover through a similar mechanism. We suggest that these pertain to RNA characteristics incompatible with efficient translation, such as short transcript length, improper RNP composition, and/or non-optimal RNA pA tail length.

Regardless the exact mechanisms, RNA 3′end tailing appears central for marking the RNA overflow, deriving from dampened NEXT-activity, for alternative downstream decay. This is eventually executed by pathways that are also operational in conventional RNA productive and destructive processes and which underscores two main principles of RNA quality control: i) It is not carried out by specific systems, but relies on redundant conventional activities, and ii) these provide a network of specialized, but also cooperative pathways, enabling cells to maintain RNA homeostasis and to survive during stress.

Methods

Cell cultures and their manipulations

Wildtype, RRP40-mAID, and ZCCHC8-mAID HeLa cells[64] were cultured in Dulbecco's modified Eagle's medium (DMEM) supplemented with 10% fetal bovine serum (FBS) and 1% penicillin/streptomycin (P/S). siRNA transfections were carried out using Lipofectamine RNAiMAX (Invitrogen) according to the manufacturer's protocol. Cells were subjected to 20 nM siRNA treatment for 3 days in all depletion experiments, except for the siRNAs targeting NXF1 and DDX39A/B,

which were restricted to 2 days due to severe cell death with prolonged depletion. For AID-mediated protein depletion, 750 μM IAA sodium salt (Sigma-Aldrich) was supplemented to cell culture medium for 6 h before cell harvest. All siRNA sequences are listed in Supplementary Table 1. For DNA damage induction, 5 μM of 4-NQO (Sigma-Aldrich) was added to cell culture media for 4 h before cell harvest.

Western blotting analysis

After harvesting, cells were counted using an automated cell counter (Invitrogen) and lysed with LDS Sample Buffer (Invitrogen) supplemented with Sample Reducing Agent (Invitrogen). Equal amounts of protein were loaded onto PAGE gels after sample denaturation at 95 °C for 15 min. Proteins were transferred to PVDF membranes, which were blocked with 5% skimmed milk in phosphate-buffered saline with 0.05% Tween 20 (PBS-T) for 1 hr at room temperature (RT), incubated with primary antibody diluted in PBS-T at 4°C overnight and followed by washing 3 × 10 min with PBS-T. Membranes were then incubated with HRP-conjugated secondary antibody diluted in PBS-T for 1 hr at RT, followed by washing 3 × 10 min with PBS-T. SuperSignal West Femto HRP substrate (ThermoFisher Scientific) was applied to membranes and signals were detected with an ImageQuant 800 (Amersham). Utilized primary antibodies are listed in Supplementary Table 2.

RNA isolation and qRT-PCR analysis

RNA was extracted using TRIzol (Invitrogen) and treated with TURBO DNase (Invitrogen) according to the manufacturer's protocol. For measuring 'all isoform' RNA levels, reverse transcription (RT) was carried out with SuperScript III reverse transcriptase (Invitrogen) using 1 μg RNA and a mixture of 20 pmol random hexamer- and 4 pmol dT_{20}.VN-primers in a 20 μl reaction at 50 °C according to the manufacturer's protocol. Subsequently, qPCR was performed using Platinum SYBR Green qPCR SuperMix-UDG (Invitrogen) in a ViiA 7 Real-Time PCR machine (Life Technologies). When measuring 'A-tailed' RNA levels, qRT-PCR was carried out similarly, except that cDNA was synthesized using 20 pmol dT_{20}.VN primers. qRT-PCR data were analyzed using GraphPad (Prism 7.0a). Utilized qPCR primers are listed in Supplementary Table 3.

In vitro transcription of spike-in RNA

DNA templates for in vitro transcription were generated by PCR using a forward primer harboring a T7 promoter sequence and a reverse primer harboring 0–5 As at its 3'end. pUC19-ERCC-00136 (for spike-in 1#) and ERCC-00136 (for spike-in 2#) plasmids were used as PCR templates[117]. In vitro transcription reactions were carried out using MEGAscript RNAi Kit (ThermoFisher Scientific) according to the manufacturer's protocol. Subsequently, RNA was purified by phenol extraction and ethanol precipitation, and its concentration was measured by a NanoDrop Spectrophotometer (ThermoFisher Scientific). The spike-in RNA mixture was prepared by first mixing spike-in 1# RNA containing 0–5 U's at the 3'ends in a ratio 5:1:1:1:1:1 as illustrated in Supplementary Fig. 2g. This mixture was further mixed with spike-in 2# RNA in a 1:1 ratio. Utilized primers are listed in Supplementary Table 3.

E-PAP treatment and measurements of U- and A-tailed RNA frequencies

To measure U-tailed RNA frequencies, 4 μg of TURBO DNase (Invitrogen) treated total RNA was mixed with 0.1 ng in vitro transcribed spike-in RNA mixture as prepared above. This RNA cocktail was treated with *E. coli* poly(A) polymerase (E-PAP, Invitrogen) at 37 °C for 30 min in 50 μL reactions, containing 1× reaction buffer, 2.5 mM $MnCl_2$, 1 U poly(A) polymerase, 2 U RiboLock RNase Inhibitor (ThermoFisher Scientific) and 1 mM ATP. E-PAP treated RNA was purified using PureLink micro RNA purification kit (Invitrogen) following the manufacturer's instructions. For the selective RT of U-tailed RNA 10 pmol of the U-tailed RNA specific primer dT_{20}.A_4 primer was used in a 20 μl reaction at 58°C to achieve high annealing specificity. RT of all RNA isoforms was carried out with 20 pmol of the dT_{20}. VN primer in a 20 μl reaction at normal PCR extension temperature of 50°C. qPCR was carried separately from cDNA synthesized with dT_{20}.A_4 and dT_{20}. VN primers. U-tailed RNA levels were normalized to levels of spike-in 1#, while the All RNA isoform levels were normalized to levels GAPDH RNA. U-tailed RNA frequencies were calculated by dividing levels of U-tailed RNA by levels of all isoform RNA. To identify the optimal U-tailed RNA-specific primer, five distinct RT primers, dT_{20}.A_1, dT_{20}.A_2, dT_{20}.A_3, dT_{20}.A_4, and dT_{20}.A_5 were tested using the in vitro transcribed spike-in RNAs. The dT_{20}.A_4 primer produced minimal background and was chosen for experiments.

To measure A-tailed RNA frequencies, RNA was treated with or without E-PAP as above. RT was carried out with the dT_{20}. VN primer for subsequent qPCR analysis. All isoform levels were measured from samples with E-PAP treatment and A-tailed RNA levels were measured from samples without E-PAP treatment by normalizing to GAPDH RNA levels. A-tailed RNA frequencies were calculated by dividing levels of A-tailed RNAs to those of all isoform RNAs.

Statistical analysis

Statistical analyses were performed using two-sided *t*-tests. Since siLuc −IAA and siLuc +IAA samples were included in multiple experiments, their statistical analyses were performed using mean values from the combined data across all relevant samples. Specifically, the following samples were combined: siLuc −IAA and siLuc +IAA data from Figs. 2a and 3a; siLuc −IAA and siLuc +IAA data from Figs. 2b and 3b; siLuc −IAA and siLuc +IAA data from Figs. 2c, e, g, 3c and 4c; siLuc −IAA and siLuc +IAA data from Figs. 2d, f, h and 3f; siLuc −IAA and siLuc +IAA data from Figs. 4e, f, g, 5a, b and Supplementary Fig. 5a; siLuc -IAA and siLuc +IAA data from Supplementary Fig. 2f, Supplementary Fig. 2k and Supplementary Fig. 4d.

RNA immunoprecipitation (RIP)

HeLa cells expressing "localization and affinity purification" (LAP) control or PHAX-LAP constructs[70,71] were treated with relevant siRNAs for 3 days. Cells were lysed in extraction buffer (20 mM Tris-HCl pH7.4, 150 mM NaCl, 2 mM EDTA, 1 mM DTT, 1 mM PMSF, 0.1% TritonX-100, supplemented with 1x proteinase inhibitor and 200 U/ml RiboLock RNase Inhibitor) and sonicated using a microtip sonicator (Branson 250). After sonication, lysates were centrifuged and clarified supernatants were incubated with Dynabeads Epoxy M270 (Invitrogen) conjugated with anti-GFP antibody and rotated at 4°C overnight. Beads were subsequently washed three times with extraction buffer. 10% volumes of beads were utilized to elute the captured protein using LDS Sample Buffer (Invitrogen) supplemented with Sample Reducing Agent (Invitrogen) for western blotting analysis. The remaining bead volumes were used for RNA extraction using TRIzol (Invitrogen).

Puromycin incorporation assay

HeLa cells were transfected with siRNAs for 48 hr. To avoid over confluent cells, resulting in less active translation, cells were reseeded at low confluency (reaching around 50% of confluency the next day) and cultured for another 24 h. 5 ug/ml of puromycin (Gibco) was added to cell culture medium for 30 min before cell harvest and western blotting analysis.

Flow cytometry analysis

siRNA-transfected HeLa cells were fixed with 70% of cold ethanol for 30 min on ice. Cells were washed with PBS and incubated in a solution, containing 50 ug/ml of propidium iodide (PI, Sigma) and 20 ug/ml of RNase A (ThermoFisher Scientific) at 37 °C for 30 min. Cells were subsequently analyzed in a CytoFLEX machine (Beckman). FlowJo 10.9.0 was used for data analysis.

RNA 3′end seq processing and read counts generation

Processing of raw reads and mapping to the genome was done as described[36], using the following versions of software: samtools v.1.6.0, bedtools v2.16, BBMAP v35.92, STAR v2.5.2b, HTSeq v0.6.0. Mapped reads were then sorted according to their type of non-aligned tail using a custom Python script. Reads were stratified via the cigar string information from bam files. Non-templated tail sequences were placed at the 5′end of reads in the utilized library preparation method (Lexogen QuantSeq REV) and thus identified with cigar strings matching the regular expressions "^.S..M" and "^..S..M" for positive- and "..M.S$" or "..M..S$" for negative-strand mappings. Further downstream analysis of total tail counts, tail-specific filtering, and the generation of coverage tracks were performed using custom Python and bash scripts.

Frequency plots

Boxplots displaying the frequencies of U-tails within samples, the representation of abundance of the individual tails' motives, and the display of U-containing reads relative to tail length within genomic and spike-in RNA were all based on counts mentioned above and generated using the ggplot2 R package.

Metagene profiles and heatmaps

Metagene profiles and heatmaps were produced using custom R scripts as in (Lykke-Andersen et al., 2021). Briefly, the rtracklayer R package was used to collect read coverage values for the window −1kb/+3kb according to the TSS. Coverage values were then binned in 50nt bins and used to generate heatmaps based on the R package ComplexHeatmap. The mean of coverage values across TUs over each bin were also computed and plotted as metagene profiles using custom R code. A 95% confidence interval of the mean coverage is displayed for each sample and was measured through 50 steps of bootstrap samplings with replacement.

Genome browser views

Genome browser views were generated using BigWig files and the R package seqNdisplayR (https://rdrr.io/github/THJlab/seqNdisplayR/).

Reporting summary

Further information on research design is available in the Nature Portfolio Reporting Summary linked to this article.

Data availability

The data supporting the findings of this study are available from the corresponding authors upon request. All high-throughput RNA-seq data used in this study were previously published[36] and are available at Gene Expression Omnibus (GEO) under accession code GSE137612. Source data for Figures and Supplementary Figs. are provided as a Source Data file. Source data are provided with this paper.

Code availability

Code and associated information for all bioinformatics analysis is available at GitHub (https://github.com/THJlab/Wu_et_al_2024) and can be downloaded from Zenodo (https://doi.org/10.5281/zenodo.14001273)[118].

References

1. Jensen, T. H., Jacquier, A. & Libri, D. Dealing with pervasive transcription. *Mol. Cell* **52**, 473–484 (2013).
2. Jacquier, A. The complex eukaryotic transcriptome: unexpected pervasive transcription and novel small RNAs. *Nat. Rev. Genet* **10**, 833–844 (2009).
3. Doma, M. K. & Parker, R. RNA quality control in eukaryotes. *Cell* **131**, 660–668 (2007).
4. Schmid, M. & Jensen, T. H. Controlling nuclear RNA levels. *Nat. Rev. Genet* **19**, 518–529 (2018).
5. Staals, R. H. et al. Dis3-like 1: a novel exoribonuclease associated with the human exosome. *EMBO J.* **29**, 2358–2367 (2010).
6. Tomecki, R. et al. The human core exosome interacts with differentially localized processive RNases: hDIS3 and hDIS3L. *EMBO J.* **29**, 2342–2357 (2010).
7. Anderson, J. S. Parker RP. The 3′ to 5′ degradation of yeast mRNAs is a general mechanism for mRNA turnover that requires the SKI2 DEVH box protein and 3′ to 5′ exonucleases of the exosome complex. *EMBO J.* **17**, 1497–1506 (1998).
8. Halbach, F., Reichelt, P., Rode, M. & Conti, E. The yeast ski complex: crystal structure and RNA channeling to the exosome complex. *Cell* **154**, 814–826 (2013).
9. Kogel, A., Keidel, A., Bonneau, F., Schafer, I. B. & Conti, E. The human SKI complex regulates channeling of ribosome-bound RNA to the exosome via an intrinsic gatekeeping mechanism. *Mol. Cell* **82**, 756–769 e758 (2022).
10. Wiederhold, K. & Passmore, L. A. Cytoplasmic deadenylation: regulation of mRNA fate. *Biochem Soc. Trans.* **38**, 1531–1536 (2010).
11. Eisen, T. J. et al. The dynamics of cytoplasmic mRNA metabolism. *Mol. Cell* **77**, 786–799 e710 (2020).
12. Malecki, M. et al. The exoribonuclease Dis3L2 defines a novel eukaryotic RNA degradation pathway. *EMBO J.* **32**, 1842–1854 (2013).
13. Chang, H. M., Triboulet, R., Thornton, J. E. & Gregory, R. I. A role for the Perlman syndrome exonuclease Dis3l2 in the Lin28-let-7 pathway. *Nature* **497**, 244–248 (2013).
14. Lubas, M. et al. Exonuclease hDIS3L2 specifies an exosome-independent 3′-5′ degradation pathway of human cytoplasmic mRNA. *EMBO J.* **32**, 1855–1868 (2013).
15. Faehnle, C. R., Walleshauser, J. & Joshua-Tor, L. Mechanism of Dis3l2 substrate recognition in the Lin28-let-7 pathway. *Nature* **514**, 252–256 (2014).
16. De Almeida C., Scheer H., Zuber H., Gagliardi D. RNA uridylation: a key posttranscriptional modification shaping the coding and noncoding transcriptome. *Wiley Interdiscip. Rev. RNA* **9**, (2018).
17. Ustianenko, D. et al. TUT-DIS3L2 is a mammalian surveillance pathway for aberrant structured non-coding RNAs. *EMBO J.* **35**, 2179–2191 (2016).
18. Okamura, M., Inose, H. & Masuda, S. RNA export through the NPC in eukaryotes. *Genes* **6**, 124–149 (2015).
19. Kohler, A. & Hurt, E. Exporting RNA from the nucleus to the cytoplasm. *Nat. Rev. Mol. Cell Biol.* **8**, 761–773 (2007).
20. McCloskey, A., Taniguchi, I., Shinmyozu, K. & Ohno, M. hnRNP C tetramer measures RNA length to classify RNA polymerase II transcripts for export. *Science* **335**, 1643–1646 (2012).
21. Ohno, M., Segref, A., Bachi, A., Wilm, M. & Mattaj, I. W. PHAX, a mediator of U snRNA nuclear export whose activity is regulated by phosphorylation. *Cell* **101**, 187–198 (2000).
22. Masuyama, K., Taniguchi, I., Kataoka, N. & Ohno, M. RNA length defines RNA export pathway. *Genes Dev.* **18**, 2074–2085 (2004).
23. Machitani, M., Taniguchi, I., McCloskey, A., Suzuki, T. & Ohno, M. The RNA transport factor PHAX is required for proper histone H2AX expression and DNA damage response. *RNA* **26**, 1716–1725 (2020).
24. Viphakone, N. et al. TREX exposes the RNA-binding domain of Nxf1 to enable mRNA export. *Nat. Commun.* **3**, 1006 (2012).
25. Carmody, S. R. & Wente, S. R. mRNA nuclear export at a glance. *J. Cell Sci.* **122**, 1933–1937 (2009).
26. Mitchell, P., Petfalski, E., Shevchenko, A., Mann, M. & Tollervey, D. The exosome: a conserved eukaryotic RNA processing complex containing multiple 3′->5′ exoribonucleases. *Cell* **91**, 457–466 (1997).

27. Wasmuth E. V., Zinder J. C., Zattas D., Das M., Lima C. D. Structure and reconstitution of yeast Mpp6-nuclear exosome complexes reveals that Mpp6 stimulates RNA decay and recruits the Mtr4 helicase. *Elife* **6**, e29062 (2017).
28. Falk, S., Bonneau, F., Ebert, J., Kogel, A. & Conti, E. Mpp6 incorporation in the nuclear exosome contributes to RNA channeling through the Mtr4 helicase. *Cell Rep.* **20**, 2279–2286 (2017).
29. Schuch, B. et al. The exosome-binding factors Rrp6 and Rrp47 form a composite surface for recruiting the Mtr4 helicase. *EMBO J.* **33**, 2829–2846 (2014).
30. Lubas, M. et al. Interaction profiling identifies the human nuclear exosome targeting complex. *Mol. Cell* **43**, 624–637 (2011).
31. Meola, N. et al. Identification of a nuclear exosome decay pathway for processed transcripts. *Mol. Cell* **64**, 520–533 (2016).
32. Silla, T. et al. The human ZC3H3 and RBM26/27 proteins are critical for PAXT-mediated nuclear RNA decay. *Nucleic Acids Res.* **48**, 2518–2530 (2020).
33. Gerlach, P. et al. Structure and regulation of the nuclear exosome targeting complex guides RNA substrates to the exosome. *Mol. Cell* **82**, 2505–2518 e2507 (2022).
34. Puno, M. R. & Lima, C. D. Structural basis for RNA surveillance by the human nuclear exosome targeting (NEXT) complex. *Cell* **185**, 2132–2147 e2126 (2022).
35. Andersen, P. R. et al. The human cap-binding complex is functionally connected to the nuclear RNA exosome. *Nat. Struct. Mol. Biol.* **20**, 1367–1376 (2013).
36. Wu, G. et al. A two-layered targeting mechanism underlies nuclear RNA sorting by the human exosome. *Cell Rep.* **30**, 2387–2401 e2385 (2020).
37. Dubiez, E. et al. Structural basis for competitive binding of productive and degradative co-transcriptional effectors to the nuclear cap-binding complex. *Cell Rep.* **43**, 113639 (2024).
38. Ogami, K. et al. An Mtr4/ZFC3H1 complex facilitates turnover of unstable nuclear RNAs to prevent their cytoplasmic transport and global translational repression. *Genes Dev.* **31**, 1257–1271 (2017).
39. Bresson, S. M., Hunter, O. V., Hunter, A. C. & Conrad, N. K. Canonical poly(A) polymerase activity promotes the decay of a wide variety of mammalian nuclear RNAs. *PLoS Genet.* **11**, e1005610 (2015).
40. Polak, P. et al. Dual agonistic and antagonistic roles of ZC3H18 provide for co-activation of distinct nuclear RNA decay pathways. *Cell Rep.* **42**, 113325 (2023).
41. Bugai, A. et al. P-TEFb activation by RBM7 shapes a pro-survival transcriptional response to genotoxic stress. *Mol. Cell* **74**, 254–267 e210 (2019).
42. Tiedje, C. et al. p38MAPK/MK2-mediated phosphorylation of RBM7 regulates the human nuclear exosome targeting complex. *RNA* **21**, 262–278 (2015).
43. Blasius, M., Wagner, S. A., Choudhary, C., Bartek, J. & Jackson, S. P. A quantitative 14–3-3 interaction screen connects the nuclear exosome targeting complex to the DNA damage response. *Genes Dev.* **28**, 1977–1982 (2014).
44. Nechaev, S. et al. Global analysis of short RNAs reveals widespread promoter-proximal stalling and arrest of Pol II in Drosophila. *Science* **327**, 335–338 (2010).
45. Kamieniarz-Gdula, K. & Proudfoot, N. J. Transcriptional control by premature termination: a forgotten mechanism. *Trends Genet* **35**, 553–564 (2019).
46. Tatomer, D. C. & Wilusz, J. E. Attenuation of eukaryotic protein-coding gene expression via premature transcription termination. *Cold Spring Harb. Symp. Quant. Biol.* **84**, 83–93 (2019).
47. Elrod, N. D. et al. The integrator complex attenuates promoter-proximal transcription at protein-coding genes. *Mol. Cell* **76**, 738–752 e737 (2019).
48. Tatomer, D. C. et al. The Integrator complex cleaves nascent mRNAs to attenuate transcription. *Genes Dev.* **33**, 1525–1538 (2019).
49. Beckedorff, F. et al. The human integrator complex facilitates transcriptional elongation by endonucleolytic cleavage of nascent transcripts. *Cell Rep.* **32**, 107917 (2020).
50. Lykke-Andersen, S. et al. Integrator is a genome-wide attenuator of non-productive transcription. *Mol. Cell* **81**, 514–529 e516 (2021).
51. Estell, C. et al. A restrictor complex of ZC3H4, WDR82, and ARS2 integrates with PNUTS to control unproductive transcription. *Mol. Cell* **83**, 2222–2239 e2225 (2023).
52. Rouviere, J. O. et al. ARS2 instructs early transcription termination-coupled RNA decay by recruiting ZC3H4 to nascent transcripts. *Mol. Cell* **83**, 2240–2257 e2246 (2023).
53. Lim, J. et al. Mixed tailing by TENT4A and TENT4B shields mRNA from rapid deadenylation. *Science* **361**, 701–704 (2018).
54. Warkocki, Z. et al. Uridylation by TUT4/7 restricts retrotransposition of human LINE-1s. *Cell* **174**, 1537–1548 e1529 (2018).
55. Kim, D. et al. Viral hijacking of the TENT4-ZCCHC14 complex protects viral RNAs via mixed tailing. *Nat. Struct. Mol. Biol.* **27**, 581–588 (2020).
56. Hyrina, A. et al. A genome-wide CRISPR screen identifies ZCCHC14 as a host factor required for hepatitis B surface antigen production. *Cell Rep.* **29**, 2970–2978 e2976 (2019).
57. Yashiro, Y. & Tomita, K. Function and regulation of human terminal uridylyltransferases. *Front Genet.* **9**, 538 (2018).
58. Yu, S. & Kim, V. N. A tale of non-canonical tails: gene regulation by post-transcriptional RNA tailing. *Nat. Rev. Mol. Cell Biol.* **21**, 542–556 (2020).
59. Liudkovska, V. & Dziembowski, A. Functions and mechanisms of RNA tailing by metazoan terminal nucleotidyltransferases. *Wiley Interdiscip. Rev. RNA* **12**, e1622 (2021).
60. Ma, X. et al. Analysis of error profiles in deep next-generation sequencing data. *Genome Biol.* **20**, 50 (2019).
61. Stoler, N. & Nekrutenko, A. Sequencing error profiles of Illumina sequencing instruments. *NAR Genom. Bioinform.* **3**, lqab019 (2021).
62. Warkocki Z., Liudkovska V., Gewartowska O., Mroczek S., Dziembowski A. Terminal nucleotidyl transferases (TENTs) in mammalian RNA metabolism. *Philos. Trans. R Soc. Lond. B Biol. Sci.* **373**, 20180162 (2018).
63. Scheer, H., Zuber, H., De Almeida, C. & Gagliardi, D. Uridylation earmarks mRNAs for degradation and more. *Trends Genet.* **32**, 607–619 (2016).
64. Gockert, M. et al. Rapid factor depletion highlights intricacies of nucleoplasmic RNA degradation. *Nucleic Acids Res.* **50**, 1583–1600 (2022).
65. Morgan, M. et al. A programmed wave of uridylation-primed mRNA degradation is essential for meiotic progression and mammalian spermatogenesis. *Cell Res* **29**, 221–232 (2019).
66. Tuck, A. C. et al. Mammalian RNA decay pathways are highly specialized and widely linked to translation. *Mol. Cell* **77**, 1222–1236 e1213 (2020).
67. Meze, K., Axhemi, A., Thomas, D. R., Doymaz, A. & Joshua-Tor, L. A shape-shifting nuclease unravels structured RNA. *Nat. Struct. Mol. Biol.* **30**, 339–347 (2023).
68. Zigackova D., Vanacova S. The role of 3′ end uridylation in RNA metabolism and cellular physiology. *Philos. Trans. R Soc. Lond. B Biol. Sci.* **373**, (2018).
69. Kurosaki, T., Miyoshi, K., Myers, J. R. & Maquat, L. E. NMD-degradome sequencing reveals ribosome-bound intermediates with 3′-end non-templated nucleotides. *Nat. Struct. Mol. Biol.* **25**, 940–950 (2018).
70. Giacometti, S. et al. Mutually exclusive CBC-containing complexes contribute to RNA fate. *Cell Rep.* **18**, 2635–2650 (2017).

71. Poser, I. et al. BAC TransgeneOmics: a high-throughput method for exploration of protein function in mammals. *Nat. Methods* **5**, 409–415 (2008).
72. De Magistris P. The great escape: mRNA export through the nuclear pore complex. *Int. J. Mol. Sci.* **22**, (2021).
73. Zinoviev, A., Ayupov, R. K., Abaeva, I. S., Hellen, C. U. T. & Pestova, T. V. Extraction of mRNA from Stalled Ribosomes by the Ski Complex. *Mol. Cell* **77**, 1340–1349 e1346 (2020).
74. Schmidt, E. K., Clavarino, G., Ceppi, M. & Pierre, P. SUnSET, a nonradioactive method to monitor protein synthesis. *Nat. Methods* **6**, 275–277 (2009).
75. Darken, M. A. Puromycin inhibition of protein synthesis. *Pharm. Rev.* **16**, 223–243 (1964).
76. Nathans, D. Puromycin inhibition of protein synthesis: incorporation of puromycin into peptide chains. *Proc. Natl Acad. Sci. USA* **51**, 585–592 (1964).
77. Ikenaga, M., Takebe, H. & Ishii, Y. Excision repair of DNA base damage in human cells treated with the chemical carcinogen 4-nitroquinoline 1-oxide. *Mutat. Res.* **43**, 415–427 (1977).
78. Malabat C., Feuerbach F., Ma L., Saveanu C., Jacquier A. Quality control of transcription start site selection by nonsense-mediated-mRNA decay. *Elife* **4**, e06722 (2015).
79. Lubas, M. et al. The human nuclear exosome targeting complex is loaded onto newly synthesized RNA to direct early ribonucleolysis. *Cell Rep.* **10**, 178–192 (2015).
80. Gable, D. L. et al. ZCCHC8, the nuclear exosome targeting component, is mutated in familial pulmonary fibrosis and is required for telomerase RNA maturation. *Genes Dev.* **33**, 1381–1396 (2019).
81. Cordiner, R. A. et al. Temporal-iCLIP captures co-transcriptional RNA-protein interactions. *Nat. Commun.* **14**, 696 (2023).
82. Wu, Y. et al. Nuclear exosome targeting complex core factor Zcchc8 regulates the degradation of LINE1 RNA in early embryos and embryonic stem cells. *Cell Rep.* **29**, 2461–2472 e2466 (2019).
83. Garland, W. et al. Chromatin modifier HUSH co-operates with RNA decay factor NEXT to restrict transposable element expression. *Mol. Cell* **82**, 1691–1707 e1698 (2022).
84. Falk, S. et al. Structure of the RBM7-ZCCHC8 core of the NEXT complex reveals connections to splicing factors. *Nat. Commun.* **7**, 13573 (2016).
85. Imamura K, et al. A functional connection between the Microprocessor and a variant NEXT complex. *Mol Cell* **84**, 4158–4174.e4156 (2024).
86. Gallie, D. R. The cap and poly(A) tail function synergistically to regulate mRNA translational efficiency. *Genes Dev.* **5**, 2108–2116 (1991).
87. Trippe, R. et al. Identification, cloning, and functional analysis of the human U6 snRNA-specific terminal uridylyl transferase. *RNA* **12**, 1494–1504 (2006).
88. Sandrock, TrippeR. & Benecke, B. BJ. A highly specific terminal uridylyl transferase modifies the 3′-end of U6 small nuclear RNA. *Nucleic Acids Res.* **26**, 3119–3126 (1998).
89. Trippe, R., Richly, H. & Benecke, B. J. Biochemical characterization of a U6 small nuclear RNA-specific terminal uridylyltransferase. *Eur. J. Biochem.* **270**, 971–980 (2003).
90. Heo, I. et al. Mono-uridylation of pre-microRNA as a key step in the biogenesis of group II let-7 microRNAs. *Cell* **151**, 521–532 (2012).
91. Faehnle, C. R., Walleshauser, J. & Joshua-Tor, L. Multi-domain utilization by TUT4 and TUT7 in control of let-7 biogenesis. *Nat. Struct. Mol. Biol.* **24**, 658–665 (2017).
92. Kim, B. et al. TUT7 controls the fate of precursor microRNAs by using three different uridylation mechanisms. *EMBO J.* **34**, 1801–1815 (2015).
93. Hagan, J. P., Piskounova, E. & Gregory, R. I. Lin28 recruits the TUTase Zcchc11 to inhibit let-7 maturation in mouse embryonic stem cells. *Nat. Struct. Mol. Biol.* **16**, 1021–1025 (2009).
94. Heo, I. et al. TUT4 in concert with Lin28 suppresses microRNA biogenesis through pre-microRNA uridylation. *Cell* **138**, 696–708 (2009).
95. Zhang, E. et al. A specialised SKI complex assists the cytoplasmic RNA exosome in the absence of direct association with ribosomes. *EMBO J.* **38**, e100640 (2019).
96. Matera, A. G. & Wang, Z. A day in the life of the spliceosome. *Nat. Rev. Mol. Cell Biol.* **15**, 108–121 (2014).
97. Neuenkirchen, N., Chari, A. & Fischer, U. Deciphering the assembly pathway of Sm-class U snRNPs. *FEBS Lett.* **582**, 1997–2003 (2008).
98. Tudek A., Lloret-Llinares M., Jensen T. H. The multitasking polyA tail: nuclear RNA maturation, degradation and export. *Philos. Trans. R Soc. Lond. B Biol. Sci.* **373**, 20180169 (2018).
99. Stewart, M. Polyadenylation and nuclear export of mRNAs. *J. Biol. Chem.* **294**, 2977–2987 (2019).
100. Passmore, L. A. & Coller, J. Roles of mRNA poly(A) tails in regulation of eukaryotic gene expression. *Nat. Rev. Mol. Cell Biol.* **23**, 93–106 (2022).
101. Huang, L. et al. The polyA tail facilitates splicing of last introns with weak 3′ splice sites via PABPN1. *EMBO Rep.* **24**, e57128 (2023).
102. Bresson, S. M. & Conrad, N. K. The human nuclear poly(a)-binding protein promotes RNA hyperadenylation and decay. *PLoS Genet* **9**, e1003893 (2013).
103. Contreras, X. et al. PAPgamma associates with PAXT nuclear exosome to control the abundance of PROMPT ncRNAs. *Nat. Commun.* **14**, 6745 (2023).
104. Meola, N. & Jensen, T. H. Targeting the nuclear RNA exosome: poly(A) binding proteins enter the stage. *RNA Biol.* **14**, 820–826 (2017).
105. Silla, T., Karadoulama, E., Makosa, D., Lubas, M. & Jensen, T. H. The RNA exosome adaptor ZFC3H1 functionally competes with nuclear export activity to retain target transcripts. *Cell Rep.* **23**, 2199–2210 (2018).
106. Shcherbik, N., Wang, M., Lapik, Y. R., Srivastava, L. & Pestov, D. G. Polyadenylation and degradation of incomplete RNA polymerase I transcripts in mammalian cells. *EMBO Rep.* **11**, 106–111 (2010).
107. Fuchs, J. C., Linden, J. F., Baldini, A. & Tucker, A. S. A defect in early myogenesis causes Otitis media in two mouse models of 22q11.2 Deletion Syndrome. *Hum. Mol. Genet* **24**, 1869–1882 (2015).
108. Heng, J. et al. Cpeb1b-mediated cytoplasmic polyadenylation of *shha* mRNA modulates zebrafish definitive hematopoiesis. *Proc. Natl Acad. Sci. USA* **120**, e2212212120 (2023).
109. Laishram, R. S. Poly(A) polymerase (PAP) diversity in gene expression-star-PAP vs canonical PAP. *FEBS Lett.* **588**, 2185–2197 (2014).
110. Yamagishi, R., Tsusaka, T., Mitsunaga, H., Maehata, T. & Hoshino, S. The STAR protein QKI-7 recruits PAPD4 to regulate post-transcriptional polyadenylation of target mRNAs. *Nucleic Acids Res.* **44**, 2475–2490 (2016).
111. Barnard, D. C., Ryan, K., Manley, J. L. & Richter, J. D. Symplekin and xGLD-2 are required for CPEB-mediated cytoplasmic polyadenylation. *Cell* **119**, 641–651 (2004).
112. Hojo, H. et al. The RNA-binding protein QKI-7 recruits the poly(A) polymerase GLD-2 for 3′ adenylation and selective stabilization of microRNA-122. *J. Biol. Chem.* **295**, 390–402 (2020).
113. Millevoi, S. & Vagner, S. Molecular mechanisms of eukaryotic pre-mRNA 3′ end processing regulation. *Nucleic Acids Res.* **38**, 2757–2774 (2010).
114. Mandel, C. R., Bai, Y. & Tong, L. Protein factors in pre-mRNA 3′-end processing. *Cell Mol. Life Sci.* **65**, 1099–1122 (2008).
115. Lee, E. S. et al. ZFC3H1 and U1-70K promote the nuclear retention of mRNAs with 5′ splice site motifs within nuclear speckles. *RNA* **28**, 878–894 (2022).
116. Parker, R. RNA degradation in Saccharomyces cerevisae. *Genetics* **191**, 671–702 (2012).

117. Schwalb, B. et al. TT-seq maps the human transient transcriptome. *Science* **352**, 1225–1228 (2016).
118. Wu G., Rouviere J. O., Schmid M., Jensen T. H. RNA 3'end tailing safeguards cells against products of pervasive transcription termination, (2024). https://doi.org/10.5281/zenodo.14001273.
119. Andersson, R. et al. Nuclear stability and transcriptional directionality separate functionally distinct RNA species. *Nat. Commun.* **5**, 5336 (2014).

Acknowledgements

We thank Claudia Scheffler for expert technical assistance and members of the T.H.J. group for fruitful discussions. Søren Lykke-Andersen, William Garland, and Andrii Bugai are thanked for their critical comments on the manuscript. The work was supported by the Novo Nordisk Foundation (ExoAdapt grant 31199 to T.H.J.) and the Danish Cancer Society (R302-A17282 to T.H.J.). G.W. was supported by a Lundbeck Foundation Postdoc grant (R347-2020-2224).

Author contributions

G.W. and T.H.J. conceived the project. T.H.J. supervised the project. G.W. performed all wet laboratory experiments. J.O.R. and M.S. performed computational analyses. G.W. and T.H.J. wrote the paper. All authors read and approved the manuscript.

Competing interests

The authors declare no competing interests.

Additional information

Supplementary information The online version contains supplementary material available at https://doi.org/10.1038/s41467-024-54834-6.

Correspondence and requests for materials should be addressed to Torben Heick Jensen.

Peer review information *Nature Communications* thanks Michal Malecki, and the other, anonymous, reviewer(s) for their contribution to the peer review of this work. A peer review file is available.